Chapter 6

Towards superlubricity of graphene on the macroscopic scale

6.1 Introduction

In 2004 Novoselov, Geim and co-workers showed in their experimental work the first two-dimensional (2D) atomic crystal – graphene – a honeycomb sheet of carbon [1, 2]. Even though the first pioneering theoretical work on graphene dates back as far as the mid-forties of the last century [3], the discovery by Novoselov *et al.* of a method to prepare graphene with minimal electronic interaction with its support has opened a new era of research. Since then the number of graphene-related scientific publications began to grow almost exponentially [4], demonstrating new properties and enabling new technologies with this special, two-dimensional material. Graphene is the lightest, thinnest and strongest material known to date [5]; also it shows record performance in terms of heat and electrical conductivity [6-11]. From a chemical point of view, defect-free graphene is unique too, being impermeable to all gases, including helium [12, 13], while at the same time being easily functionalized with various chemical species [14]. Therefore, the past decade has also witnessed significant effort into technology-oriented research, exploring new graphene applications – from new types of transistors [15, 16] to applications in solar cells [17] and in biomedical devices [18].

As graphene forms a natural constituent of graphite and graphite is commonly used as a solid lubricant, the frictional properties of graphene have attracted attention too [19, 47-52]. For instance, nanoscale friction force microscopy measurements on graphene supported by copper foils [20, 21] or by silicon oxide [22, 47] demonstrated a significant lowering of the friction forces on the graphene-covered patches with respect to graphene-free parts of these substrates. By virtue of recent developments in graphene growth techniques [23, 24], it is now becoming possible to study the impact of the presence of a graphene monolayer beyond the atomic scale, for example for single contacts in the micrometer regime and for macroscopic ensembles of large numbers of contacts. In one of the early works in this area, Kim *et al.* showed superior friction and adhesion properties of single-monolayer graphene films grown by chemical vapor deposition (CVD) on Cu and Ni substrates [28]. Later, Berman *et al.* demonstrated that graphene helps significantly to minimize wear and friction at the macroscale between a steel ball and graphene-covered solid substrates in various gas atmospheres [25, 26]; Mao *et*

al. measured a 10-fold reduction of the friction coefficients for Ag-based electrical contacts in the presence of graphene [27]. In later work, Berman *et al.* achieved extremely low friction, which they ascribed to macroscale 'superlubricity' enabled by the formation of so-called graphene nanoscrolls at the interface between a DLC coated substrate and a graphene coated counter surface [29]. They have demonstrated a sustained reduction of the friction coefficient to 0.004, which may be very promising for future lubrication technology.

Unfortunately, the term 'superlubricity' is used in the friction community with more than a single meaning. Whereas it often simply indicates extremely good lubrication, for example in the case of the nanoscrolls of ref. [29], the term 'superlubricity' was coined by Hirano *et al.* [30-33] to indicate a friction regime when 'two contacting surfaces can slide with no resistance', as the result of a mismatch between their lattices, for example when they are twisted out of registry. A perhaps more meaningful term to cover this narrower definition is 'structural lubricity'. In this chapter (as well as in the rest of this PhD thesis) we will use both terms, but always in the narrower context of a lattice mismatch. Hirano *et al.* demonstrated that the friction between two cleaved mica surfaces exhibits a modest variation between commensurate and incommensurate orientations of the two mica lattices. Later, electron microscopy observations on MoS_2-lubricated contacts suggested that a similar mechanism may be at play between the differently oriented MoS_2 flakes in such contacts [34]. Further evidence for structural lubricity on the nanometer scale has been acquired for e.g. graphene [46] and for graphite flakes [35]. In the latter case, Dienwiebel *et al*. demonstrated directly how friction becomes ultra-low when a graphite-graphite interface is rotated out of registry. The friction force is only high when the lattices can lock in, which occurs every 60° of rotation, corresponding to the rotation symmetry of the graphite lattice [83] Since superlubricity is intimately related to the crystalline structure of the contacting materials, one may expect that it would be sensitive to the crystalline quality of the materials, for example to the density of lattice defects. If this is indeed the case, this is important for practical applications, for which the contact sizes are usually much larger than the nanocontacts of the early demonstration experiments. So far, the largest contacts for which structural lubricity has been demonstrated are graphite-graphite contacts with areas of a few hundred μm^2 [36, 37].

A promising candidate material that might be effective as a low-friction coating, by preserving the effect of structural lubricity even on the macroscopic scale, is graphene. One of the great advantages of a graphene coating could be that it smoothly decorates the natural irregularities of the substrate on which the graphene is either grown or to which it is transferred. Imperfections in the substrate, such as atomic steps, grain boundaries and point defects are covered such that we may hope their effect on friction to be minimized. A graphene coating would further avoid direct atomic contact between the substrates and thus prevent the formation of chemical bonds that would otherwise lead to high friction and wear. Nowadays, graphene is produced over areas that are large enough to be used as a macroscopic-scale coating, albeit that the structural quality of this graphene is still far from perfect. Nevertheless, graphene may be regarded as one of the most promising candidate materials to achieve superlubricity at the truly macroscopic scale.

In this chapter, we discuss the results of our experiments towards superlubricity on the macroscopic scale with commercial CVD-grown graphene on polycrystalline Cu substrates. Also, we conducted some basic, 'Leonardo-da-Vinci style' [38] experiments to study lubrication properties of monolayer graphene on cm^2–scale sliding contacts. Finally, we discuss the oxidation behavior of graphene-coated substrates under ambient conditions and the local effect of that oxidation on the friction properties.

6.2 Experimental

For our experiments, we used high-quality, single-monolayer graphene samples that were commercially produced by Applied Nanolayers (ANL) BV [39]. In ANL's production process, graphene is grown by CVD on polycrystalline copper films. These films are formed by sputter deposition of copper on sapphire (111) wafers (diameter 51 mm, thickness 750 μm). The copper grains in the film showed a strong preference for the (111) surface orientation. We used these graphene samples both as the stationary, lower body in our sliding experiments and as the upper body, the slider. For these experiments, the sliders had to be smaller in size than the lower bodies; we prepared them by dicing graphene-coated wafers into squares with dimensions of $1 \times 1\ cm^2$ and a mass of $m = 0.16\ g$. Dicing was performed under cleanroom conditions in order to avoid dust contamination. Prior to dicing, the wafers were spin-coated with S1805 photoresist [40], in order to protect them against small-particle debris that originates from the dicing itself. The photoresist was spin-coated at 4000 RPM, and baked out at 130°C for 60 sec in air. The wafers were diced with a rotary dicing machine using a precision diamond blade VT-07 [41] at 20000 RPM. Afterwards, the photoresist was washed off from the diced samples in N-methyl-2-pyrolidone at 80°C during 5 minutes. Finally, the samples were quickly rinsed in demi-water and dried with N_2 gas. The graphene quality was monitored before and after this complete dicing operation with optical microscopy and Raman spectroscopy. These control measurements did not reveal any measurable increase in defect density in the graphene, no transferred contamination and no signs of damage. Therefore, we assume that the graphene quality remained close to that of the original graphene coating. It is also important to indicate that all friction experiments were conducted shortly after (several days) the samples were coated with graphene and prepared in the cleanroom. Some samples that were exposed to air for longer times (up to a few months) became oxidized and this effect will be discussed separately.

For comparison, we have performed friction experiments not only with graphene-coated substrates but also with uncoated copper films. These were prepared and diced following precisely the same protocol as the graphene-coated samples.

Similar to the experiments with DLC coatings, reported in Chapters 4 and 5, the macroscopic friction measurements of this Chapter were performed with the Bruker UMT-1 Universal Mechanical Tester. For details of this instrument, see Chapter 4. In our experiments, the lower of the two contacting bodies was mounted directly on the substrate table of the microscope, while the smaller counter-sample was positioned on top of it under its own weight of $1.56\ mN$. The normal force could be increased beyond this level by placing an additional weight on top. Lateral (friction) forces were measured while pushing from one of the sides against the counter-sample at a fixed driving speed of 5 $\mu m/sec$. In another type of measurements, we imposed a continuous in-plane rotation of the counter-sample with respect to the lower body at a speed of $0.01\ deg/sec$. To this end, we rotated the stage with the lower body mounted in its center. The square counter-sample was placed in the middle of the substrate. The pusher block of the UMT was placed against one of the sides of the counter-sample, keeping the counter-sample from rotating with the substrate and measuring the force (torque) that was required for that.

In addition to measurements on the macroscale, we have also conducted friction measurements on the nanoscale. These were done with a Bruker AFM Icon, using V-shaped Si_3N_4 probes (DNP-10). The relative humidity could be controlled by flushing the AFM chamber with nitrogen vapor from a liquid nitrogen reservoir. The height of the tip was measured to be $h = 4.0 \pm 0.5\ \mu m$, the length of the beams of the cantilever $L = 210 \pm 2\ \mu m$ and the angle between them $\theta = 60^{\circ} \pm 0.5^{\circ}$. The normal spring constant k_N for each cantilever was obtained from a measurement of its natural frequency (for the method see [61]). The lateral spring constant k_L of was calculated based on the measured value of k_N and the geometry of the cantilever [55, 62]:

$$k_L = \frac{2}{[6cos^2\theta + 3(1+\nu)sin^2\theta]}\left(\frac{L}{h}\right)^2 k_N. \qquad (6.1)$$

Here, ν is the Poisson ratio (for SiN, $\nu = 0.27$). Typical values of k_N and k_L for the employed cantilevers are in the range of $0.05 - 0.2\ N/m$ and $35 - 120\ N/m$, respectively. We followed the lateral and normal force calibration procedure of refs. [55, 60]. The normal force was determined on the basis of the measured

voltage response of the photo-diode V_N during normal bending of the cantilever in contact with the substrate. Force-distance curves were recorded in order to determine the normal sensitivity S_N. The resulting force value is then given by:

$$F_N = k_N S_N V_N. \tag{6.2}$$

To calculate the lateral force, we used a relation between the lateral S_L and normal sensitivity S_N. According to [61] the two are related by:

$$S_L = \frac{3}{2} k_L \frac{h}{L} S_N. \tag{6.3}$$

Thus the lateral force can be found

$$F_L = k_L S_L V_L, \tag{6.4}$$

where V_L is the relative change in voltage signal from the photo-diode due to lateral bending of the cantilever.

We have also conducted micro-Raman spectroscopy experiments. These were conducted with a laser wavelength of 514 nm and a spot size of ~1 μm. SEM inspection was performed with a FEI Verios scanning electron microscope.

6.3 Experimental results

Figure 1 represents typical results of the SEM and Raman inspection of a freshly coated graphene sample. Because of highly homogeneous character of the graphene film, the SEM image shows hardly any contrast and the only clearly visible structures are related to grain boundaries (GB) in the underlying copper film (Fig. 6.1a). In turn, the Raman spectrum (Fig. 6.1b) provides information on the defects in the graphene layer itself (D-band around 1360 cm^{-1}), the in-plane vibrations of the sp^2-bonded carbon atoms (G-band at 1595 cm^{-1}), and the stacking order in the case of multilayer graphene (2D-band around 2730 cm^{-1}). The symmetric and sharp 2D-peak indicates that this is a graphene monolayer [42, 43]. The peak intensity ratio of $I_{2D}/I_G > 1$ also indicates the presence of only monolayer

graphene, albeit that this ratio strongly depends on the laser excitation energy and is sensitive to the details of the binding between the graphene layer and the substrate [44]. It was demonstrated that in the green laser range (an excitation energy of $2.2 \div 2.4\, eV$) the intensity of the Raman resonance profile becomes stronger than at higher energies (above $2.8\, eV$). This effect is related to the photoluminescence band of the Cu substrate. In our experiments, we employed a laser wavelength of $514\, nm$, which corresponds to the excitation energy of $2.41\, eV$. The acquired spectrum is in a good agreement with the literature [42-44]. The spectrum in Fig. 6.1b is shown after the subtraction of the background from the luminescence from the copper substrate.

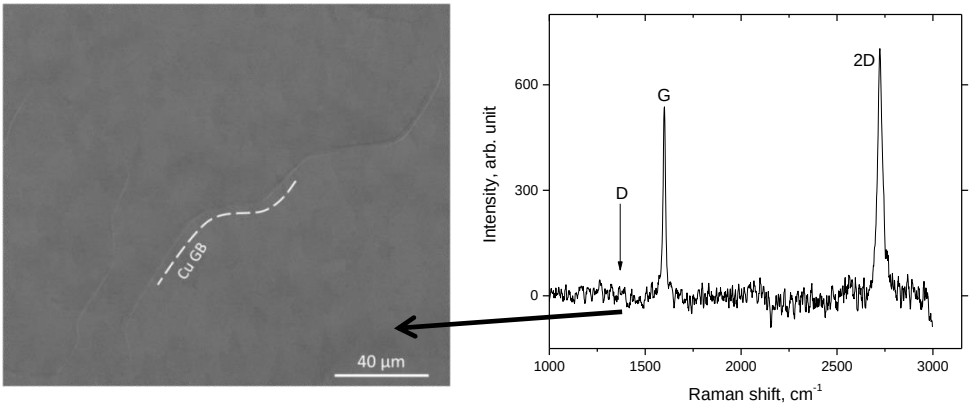

Figure 6.1. SEM image (a) and Raman spectrum (b) of CVD grown graphene on top of a polycrystalline Cu film. The dashed line in (a) highlights part of a grain boundary in the copper film. The absence of a D peak in (b) indicates the negligible density of structural defects in the graphene lattice; the ratio between the heights of the G and 2D peaks and their positions correspond to those for monolayer graphene.

Figure 6.2 shows friction measurements for two different interfaces, namely the interface between two copper surfaces and the interface between two samples coated with monolayer graphene. These measurements were performed in ambient, in a relative humidity of 45%. Note, that the formation of an oxide film at the surface of copper proceeds immediately after its exposure to ambient air and after 1 hour of exposure the typical thickness of the Cu_2O already amounts to $2.5 \pm 0.2\, nm$ [45]. It has also been demonstrated that the thickness of the copper

native oxide finally stabilizes after 66 days of exposure and reaches a thickness of $5.2 \pm 0.5\,nm$. Therefore, we refer to the copper-on-copper results as Cu_2O on Cu_2O. The effect of the graphene coatings is dramatic. They reduce the friction coefficient by more than a factor 3 ($\mu_d = 0.14$) with respect to the uncoated samples ($\mu_d = 0.43$).

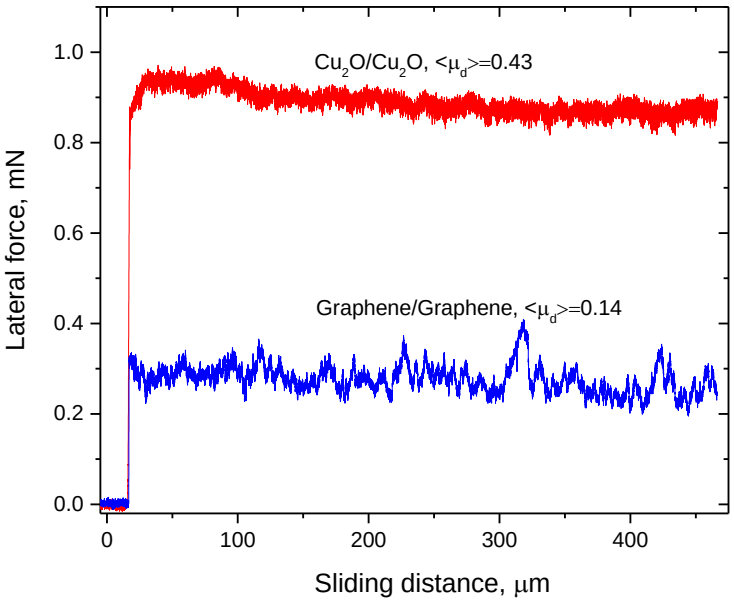

Figure 6.2. Comparison of the friction forces between two samples coated with monolayer graphene (blue curve) and two oxidized copper samples without graphene (red curve). Sliding speed = $5\ \mu m/sec$, $F_N = 2\ mN$, *and* $RH = 45\%$.

Figure 6.3 represents the initial stages of the same sliding experiments as those in Fig. 6.2, showing the transition from the static situation, with the slider at rest, to steady sliding motion for the graphene/graphene and native oxide Cu_2O/Cu_2O friction pairs. While the transition to steady sliding requires the overcoming of a static friction barrier for the Cu_2O/Cu_2O case, the graphene/graphene pair seems to exhibit no difference between the static (μ_s) and dynamic (μ_d) coefficients of friction. Both measurements were done after the sliding surfaces spent 2 min in rest.

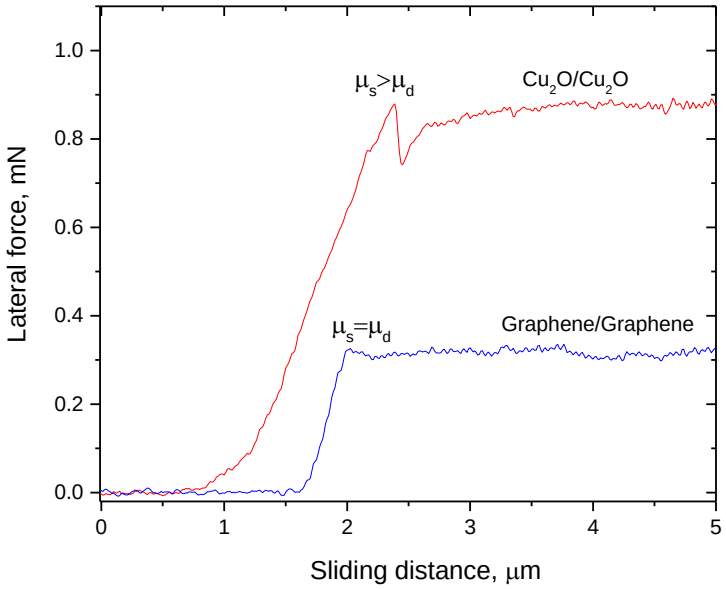

Figure 6.3. Transition from static friction to steady sliding (same data as Figure 6.2, on expanded horizontal scale) for two samples coated with monolayer graphene (blue curve) and two oxidized copper samples without graphene (red curve). Sliding speed = 5 $\mu m/sec$, $F_N = 2\ mN$, *and* $RH = 45\%$.

An example of a measurement of the frictional torque during the relative rotation of two graphene-coated samples is shown in Fig. 6.4. The substrate was sequentially rotated over 120° in the clockwise and counterclockwise directions. The mean value of the frictional torque is in full agreement with the force measured in the linear sliding geometry of Figs. 6.2 and 6.3, indicating that also in the rotation measurements, the graphene coatings reduce friction. Naively, one might have expected that, following the scenario of structural lubricity [33-36], the friction signal should display a characteristic variation with rotation with a period of 60°, between a low level for most angles and a pronounced maximum for the angels at which the two contacting graphene lattices would align and lock in. The friction data in Fig. 6.4 do not show such a periodic signature. We have used a standard rotational rheometer (Anton Paar DSR301) to perform additional experiments in search of rotational symmetry in the friction between the lattices of macroscopic graphene coatings [82]. The results from these rheometer experiments

were similar to those in Fig. 6.4; again we find no evidence in the forces for the periodic alignment of the graphene lattices. We will put forward an explanation for the absence of a periodic variation in the friction forces in the Discussion section.

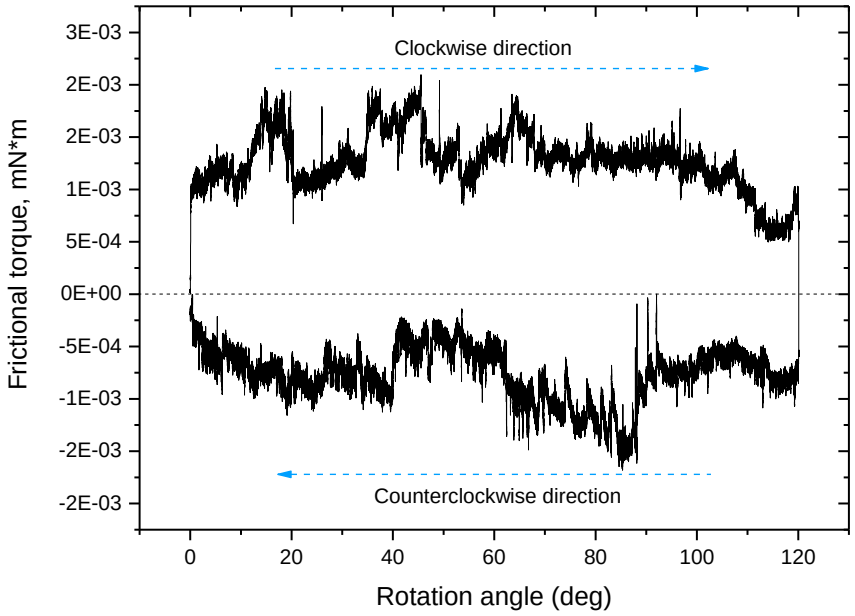

Figure 6.4. Frictional torque measured during the forced rotation of a graphene/graphene interface. Rotation speed of the substrate $0.01\ deg/sec$, $F_N = 2\ mN$, *and* $RH = 2\%$.

Not only the copper surfaces responded to the atmosphere, but we found that also the surface topography of our graphene samples slowly evolved under ambient conditions. A comparison of AFM-images on a graphene-covered sample before and after 2 months in air is presented in Figs. 6.5a and b. Figure 6.5c shows an optical micrograph of the same sample after 2 months in air. The AFM image in Fig. 6.5a is characteristic for high-quality graphene on relatively flat and smooth copper. A modest overall height variation is visible and individual steps of the copper substrate can just be distinguished. Figure 6.5b shows the same area with the same features. In addition, a fine network of protruding lines and islands is visible. The image of Fig. 6.5c shows a similar network, where the optical contrast

has changed. We associate these slow changes with oxidation of the copper substrate. Structurally perfect graphene is impenetrable for oxygen, and structural defects in the graphene, such as the graphene grain boundaries (GGBs) form the only locations where oxygen can pass and reach the copper. This gives rise to a slow, diffusion-limited oxidation that sets in at the GGB and spreads out sideways to oxidize the copper under the graphene. The optical image also contains a grain boundary in the copper film that shows up with a different contrast than the oxide-decorated GGBs. Note, that the orientation of the GGBs is independent of the orientation of the Cu steps and they even cross Cu GBs (Fig. 6.5c). The black dots in the optical micrograph (Fig. 6.5c) are regions of bulk copper oxide that have grown in height above the sample surface and are not dressed with graphene anymore. This is concluded from Raman measurements conducted at these locations. Presumably, they are formed at places along the GGB with the highest defect density, which enables a relatively high oxidation rate [54].

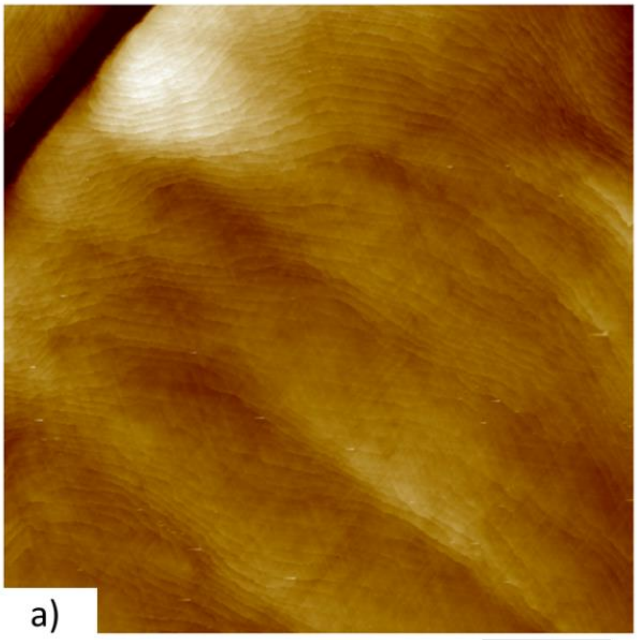
a)
10.0 µm

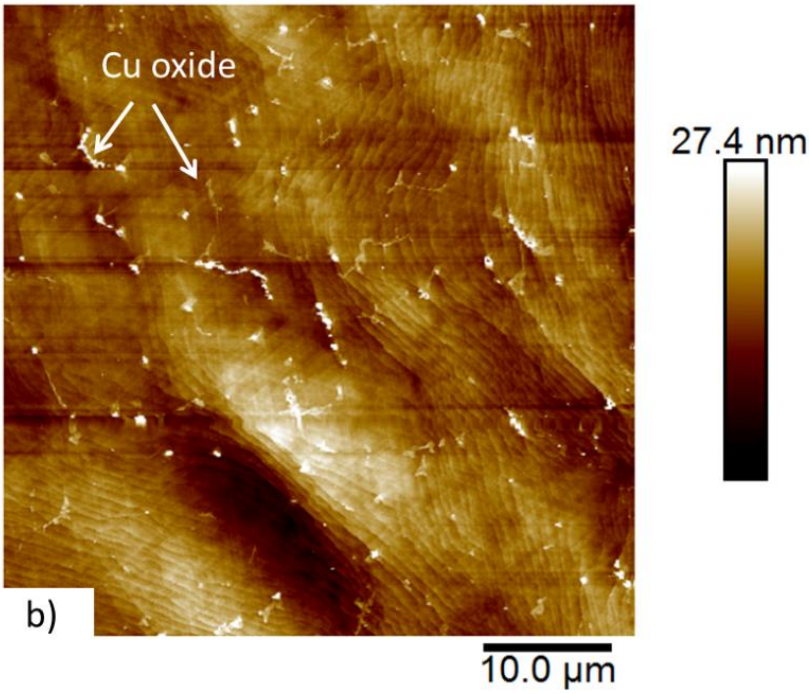
Cu oxide
27.4 nm
b)
10.0 µm

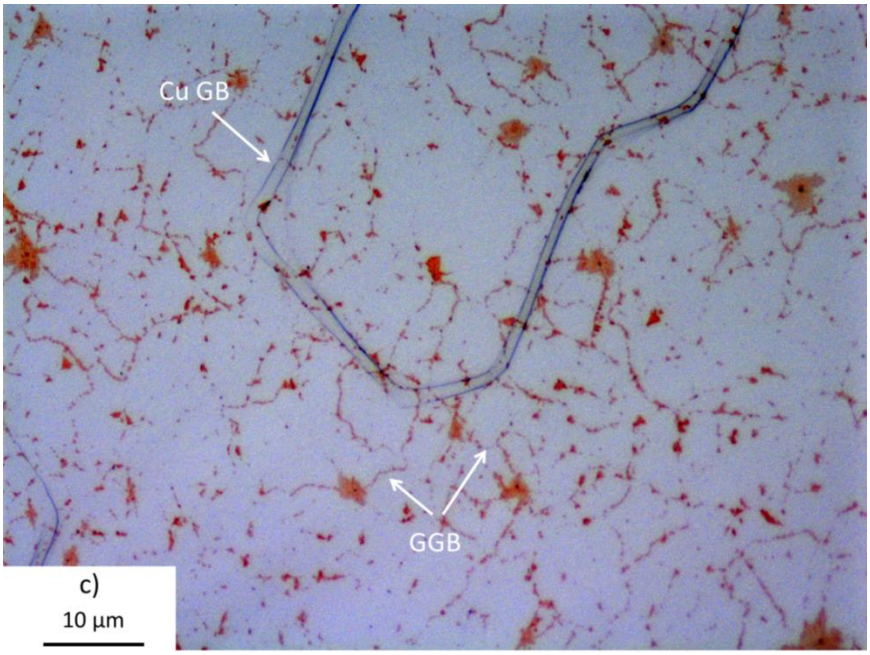

Figure 6.5. AFM and optical images of a graphene-covered copper surface. (a) AFM image shortly after coating with graphene (a few days exposed to air). (b) AFM image of nearly the same surface region after 2 months of exposure to air. Note the decoration of the network of GGBs with oxidized copper underneath. (c) Optical micrograph after 2 months of exposure to air, showing the network of oxide-decorated GGBs. The image also shows a Cu GB. Note, that the orientations of the GGBs do not seem to be affected by the orientation of the Cu GB.

In order to further characterize the slow oxidation, we acquired Raman spectra on the oxidized areas of the copper substrate close to a GGB and compared them with spectra taken on the unoxidized areas (at a distance from the GGBs). An example of such a comparison is presented in Fig. 6.6. The two spectra in Fig. 6.6 were taken with a rather low laser power of 8 μW, which corresponds to 0.1% of the laser's nominal power. This was necessary to avoid heat damage produced by the laser to the copper oxide, but it resulted in a weakening of the signal to noise ratio in both spectra (Fig. 6.6).

In the regions where the copper oxidation is visible, we find that both the G- and the 2D-band are 'redshifted' with respect to the bands for 'regular' graphene on bare, unoxidized copper. The average position of the G-band shifted from 1592 cm^{-1} to 1585 cm^{-1}, and that of the 2D-band from approximately 2727 $cm^{-1}$to 2680 cm^{-1}. In spite of these changes, we could not detect the D-band that would be

associated with defects in this graphene on top of the oxidized copper. The intensity ratio of the 2D- and G-bands on the oxidized copper was $I_{2D}/I_G = 2.3$, which is much higher than the ratio of $I_{2D}/I_G \approx 1$ for unoxidized areas. Some arguments for the increased peak intensity ratio follow in Discussion section. Previously, a similar redshift of the characteristic Raman bands was reported for graphene-coated copper samples, which were oxidized on purpose with ultraviolet radiation (UV) in oxygen atmosphere [54, 58]. In turn, the redshift of the characteristic bands is known to indicate tensile strain in the graphene. In our case, there is a natural reason for such strain, in view of the increased volume below the graphene due to the oxidation of the copper [58]. The redshifts in Fig. 6.6 correspond to approximately 0.5 to 1.5% of tensile strain [57].

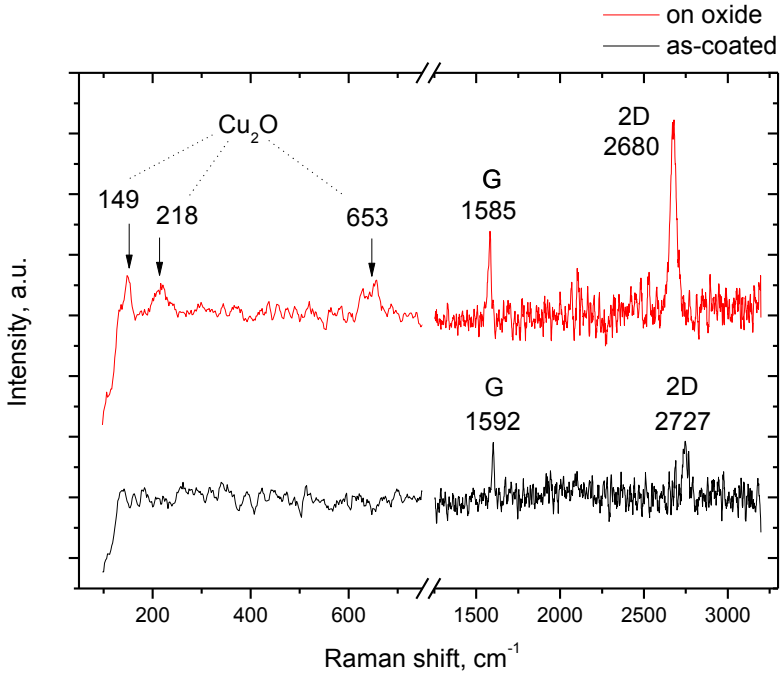

Figure 6.6. Raman spectra of graphene on copper (black line) and graphene on a region with oxidized copper (red color), taken with a laser excitation wavelength of 514 *nm. Note the 'redshift' of the G- and D-bands on the oxidized substrate. Also, there are three extra peaks at* 149, 218, *and* 653 cm^{-1}, *associated with Raman scattering on copper oxide (Cu2O). The spectra are vertically shifted for clarity.*

Figure 6.7 represents an example of a $2x2\ \mu m^2$ region of the locally oxidized sample, inspected with both AFM and FFM. In the center of Fig. 6.7a there is a copper oxide island with an average height of $2.5\ nm$ (Fig. 6.7b). On the left and right of it, the white arrows point at a GGB that runs across the oxide island. The GGBs typically observed on the studied samples show up as a protruding line with a height in the range of 0.3 to $1.5\ nm$. This elevation along the GGBs can be presumably due to (i) elastic strain and mechanical deformation as a result of the lattice mismatch induced by the two different grains [53, 59] or (ii) growth of the copper oxide under the GGB. In the example of Fig. 6.7, the GGB is measured to be $0.6\ nm$ in height (Fig. 6.7c). The GGB is difficult to distinguish on the island itself, because of the relatively high roughness. Figures 6.7d and e present the FFM scans taken in the forward (left-to-right) and reverse (right-to-left) directions, respectively. Interestingly, the FFM measurements indicate that the friction force is lower on the graphene areas below which the copper is oxidized. Both friction signals indicate a relative increase of the lateral force everywhere along the GGB, which we ascribe to the protruding height of the GGB, and possibly also to local oxidation of the graphene – something that Raman spectroscopy would not be sensitive to at this scale, due to relatively large laser spot size.

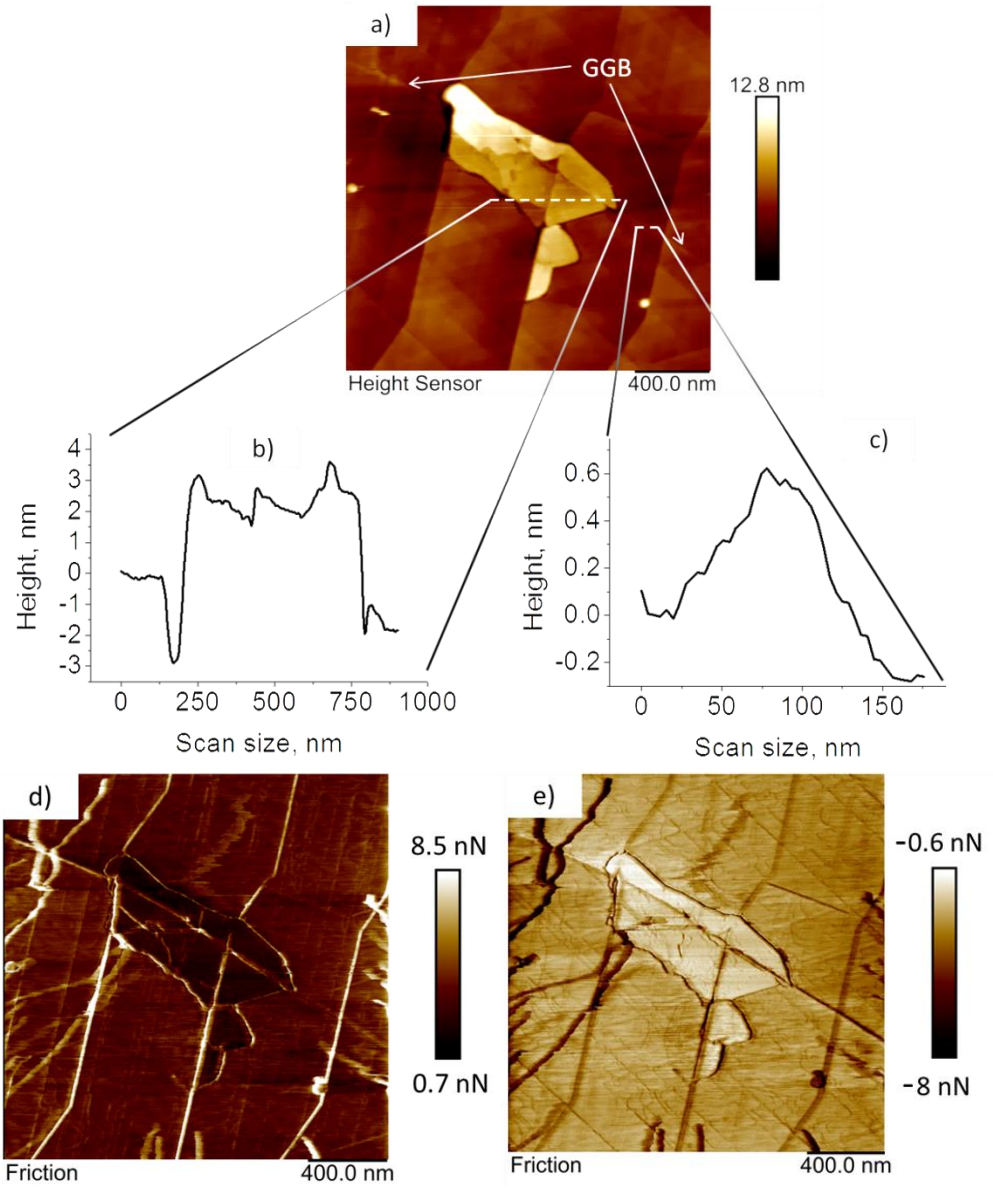

Figure 6.7. AFM and FFM scans of a region on a graphene-covered sample that contains an oxidized area of copper. The GGB that has served as the starting point for this oxidation can be recognized. a) AFM image; b) height profile across the oxide island; c) height profile across the GGB; d,e) lateral force maps of the same area measured in trace and retrace directions respectively. Scan area is $2x2\ \mu m^2$*, normal force* $F_N = 20\ nN$*, scan speed is* $1\ \mu m/sec$*,* $RH\ =\ 45\%$.

The dependence of the lateral force on the normal force for graphene on copper and graphene on copper oxide is presented in Figure 6.8 for another copper oxide island than the one in Fig. 6.7. The scan area was fixed to $1.5x0.5\ \mu m^2$, with the oxide region in the center. The measurement was conducted in ambient in the range of normal forces from $F_N = 23.7$ to $33.0\ nN$, with a cantilever with normal and lateral spring coefficients of $0.09\ N/m$ and $38\ N/m$, respectively. The lateral force values were calculated based on averaged data taken along the white dashed line that was chosen randomly in the scan image (Fig. 6.8). It is clear from the two curves in Fig. 6.8, that their slopes are very different. These slopes correspond to the two friction coefficients that we determined by linear regression to the measured data (Fig. 6.8e). The friction coefficient obtained in this way on graphene/copper oxide areas is $\mu = 0.034 \pm 0.02$, while it is $\mu = 0.093 \pm 0.02$ on the graphene/copper areas. Again, a local maximum in the lateral force was observed across the GGB (Fig. 6.8c,d).

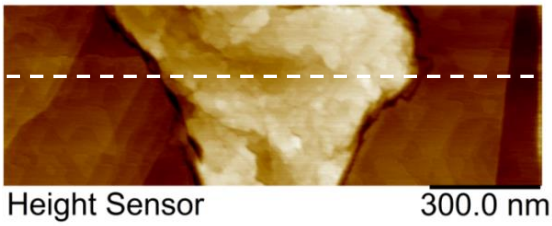
Height Sensor
300.0 nm

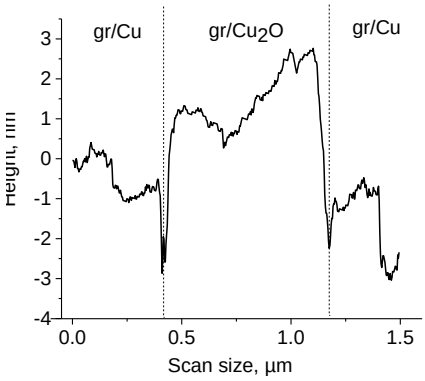
gr/Cu
gr/Cu2O
gr/Cu
Height, nm
3
2
1
0
-1
-2
-3
-4
0.0
0.5
1.0
1.5
Scan size, μm

a) b)

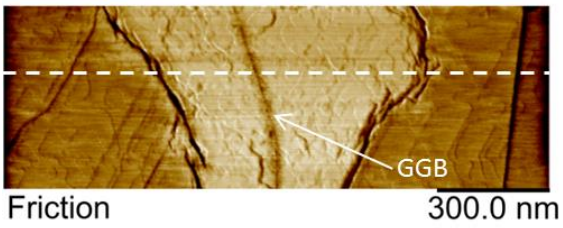
GGB
Friction
300.0 nm

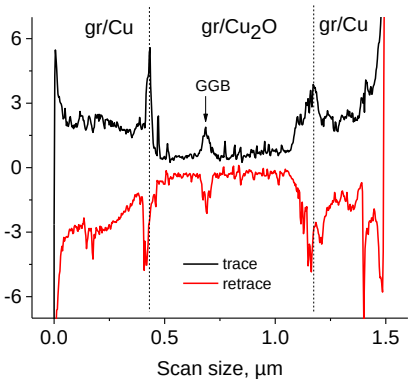
gr/Cu
gr/Cu2O
gr/Cu
GGB
6
3
0
-3
-6
trace
retrace
0.0
0.5
1.0
1.5
Scan size, μm

c) d)

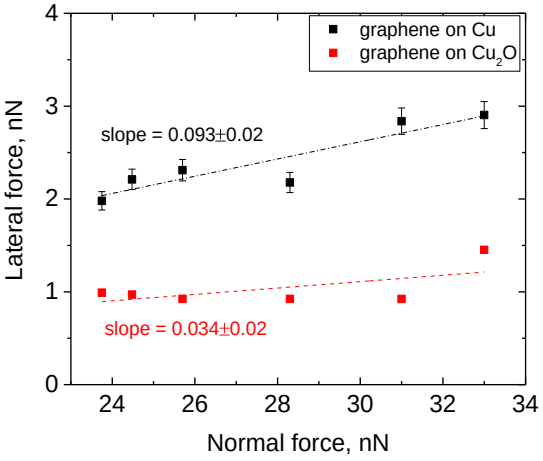

e)

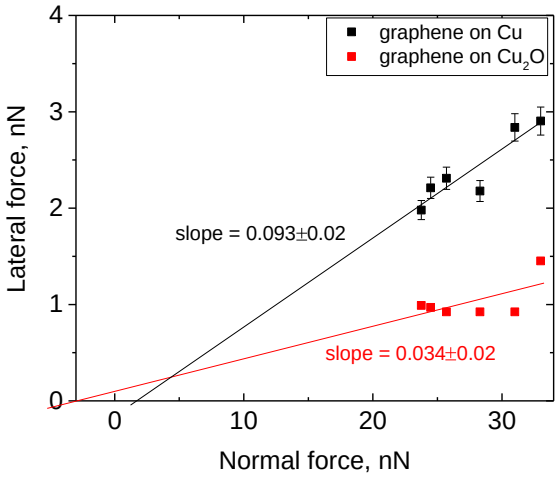

f)

Figure 6.8. Quantitative comparison of friction properties of graphene on copper (gr/Cu) and graphene on copper oxide (gr/Cu2O). a) AFM image of a $1.5x0.5\ \mu m^2$*, region of graphene-coated copper, with a copper oxide island in the center; b) height profile across the copper oxide island taken along the dashed line in a); c) lateral force image of the same area taken in the retrace (right to left direction) at* $F_N = 23.7\ nN$*; d) lateral force profile taken from trace and re-trace scans along the dashed line in a); e) dependence of the (absolute value of the) lateral force on the normal force for graphene/copper and graphene/copper oxide, measured along the same dashed line in a) for normal forces in the range of* $F_N = 23.7 \div 33.0\ nN$*; f) extrapolation of the linear data fit from e) to the point of origin* (0,0).

6.4 Discussion

6.4.1 Graphene as the thinnest lubricant

We have demonstrated the suppression of the dynamic (sliding) friction coefficient by approximately a factor 3 and also the significant reduction of the static friction coefficient by applying only a single monolayer of graphene on both contacting surfaces. We have used flat graphene samples that were obtained by direct graphene growth on copper substrates and that did not undergo any subsequent transfer to another substrate. This means that in our experiments the contact between the sliding copper surfaces was fully determined by graphene/graphene interaction. High quality and complete coverage by graphene form key elements in our explanation of the observed frictional behavior. We interpret our observations as evidence that most, if not all, of the copper asperities in our contacts were "shielded" by the graphene and thus protected from direct formation of metal-metal bonds. Therefore, the interaction between the sliding surfaces was changed from chemical to purely physical [63]. As perfect graphene has an intrinsically low surface free energy, it results in a significant lowering of the interfacial adhesion and a correspondingly strong lowering of the shear strength of the interface. This is illustrated by recent density functional theory (DFT) calculations, which show that even partial coverage of iron surfaces with graphene ribbons may reduce the adhesion between them by almost a factor 6 [63]. This is confirmed by the experimental observations in ref. [25] for steel surfaces decorated with graphene flakes. Next to the reduced adhesion, also structural lubricity, i.e. the lubricating effect of the mismatch between randomly oriented graphene or graphite lattices [35], should be expected to contribute greatly to the reduction of the friction force. Another effect that graphene may introduce, is that the elastic behavior of the graphene coating may reduce the plastic penetration depths of the asperities on the copper surfaces, thus enhancing the load capacity of the graphene-decorated copper-copper interface [64]. The final element to add is that the graphene-covered copper surfaces should be expected to suppress the increase in the friction coefficient that is typical for bare copper surfaces in humid environments. Graphene should reduce the tendency for capillary condensation of water between the contacting surfaces, since it is less hydrophilic than copper

oxide. In addition, it was demonstrated that adding graphene to a Cu surface may increase the mobility of water droplets due to depinning of water contact lines, in contrast to hydrophilic copper oxide surface [61]. Together, these effects should reduce the effect that capillary water bridges have on the confined areas of contact between graphene/copper samples. All of these elements contribute to our expectation that a graphene-coating reduces the friction between copper surfaces. More systematic experiments are needed in order to investigate how strong each of these effects is.

Not only the dynamic friction force is reduced by the graphene, also the static peak that usually accompanies the onset of sliding is strongly affected; within the noise level of our measurement, it is absent completely when the graphene coating is present. Also this is no surprise. Normally, capillary water bridges and structural and geometrical pinning effects between the contacting asperities add significantly to the static friction threshold [67]. All these effects are strongly suppressed by the presence of the graphene coating.

An important question is, how long these unique lubrication properties of the ultrathin graphene coating should be expected to last. Like any other material, graphene exhibits a certain wear rate, which determines its lifetime as a lubricant [72]. The beneficial role of the graphene should hold at least as long as it remains present and the high structural quality of the graphene is maintained on those parts of the surfaces that are in mechanical contact. Local damage of the graphene layer under load should lead to the accumulation of carbon dangling bonds. These should result in higher interfacial adhesion due to both the direct cross-linking between damaged graphene layers and the bridging via water molecules and hydrocarbon groups that can bind easily to these dangling bonds [19, 65-66]. In particular, Berman *et al*. [66] demonstrated significant reduction of the graphene wear rate by means of passivation of the dangling bonds with hydrogen atoms from the hydrogen gas atmosphere, which could make graphene extra effective for lubrication in realistic applications. In our study, we have examined the wear of graphene by means of Raman spectroscopy. For this, we have conducted sliding experiments only over relatively short distances of typically several millimeters. In the Raman spectra after sliding, no significant increase of the D-band intensity was detected. Even though this result is highly encouraging, we can regard it as no

more than a preliminary result, until we have conducted a more systematic Raman study over larger areas of the studied substrates and after more extensive sliding.

It may come as a surprise that graphene is so effective on copper substrates, in view of the weak, Van-der-Waals type bonding that characterizes the interaction between the graphene and the copper. Graphene makes chemical bonds only to metals as Co, Ni, Pd and Fe [63, 68-71] that have incompletely filled *d* bands. Graphene binds to a Cu substrate purely by physisorption, because the *d* band of Cu is fully occupied. Therefore, the adhesion energy of graphene on copper is much lower (up to a factor 6, compared to Ni and Fe) [63, 69]. As a result, one might anticipate significant distortions of the graphene on copper under the combination of normal and shear forces, which would make the graphene much more vulnerable to wear on this substrate. Nevertheless, the millinewton range of normal loads and the millimeter range of travel distances used in our experiments has not resulted in any directly observable wear. We also did not measure any significant reduction in the lubricating effect of the graphene. An increase in the friction coefficient would have been a sign of the local detachment or modification of the graphene in the actual contact regions.

6.4.2 Towards superlubricity at the macroscale

The superlubric behavior that was demonstrated for graphitic materials at the nano- and microscale [35, 36] has served as the motivation to use CVD-grown graphene in order to extend this effect even further, to the macroscopic scale. One of the questions in this experiment is whether or not the structural quality of the graphene could be sufficiently high to use it for this purpose. The experiments in this Chapter clearly demonstrate a significant reduction of the static and dynamic friction coefficients between two surfaces resulting from the presence of single-monolayer graphene on both contacting surfaces. An important question is to what extent this friction reduction derives directly from superlubricity, i.e. from the friction-lowering effect introduced by the mismatch between the contacting graphene lattices. In the previous section, we have provided several other reasons for friction to be low in the presence of a graphene coating. In the experiment of Fig. 6.4, we have tried to obtain direct evidence of the lattice-mismatch scenario of structural lubricity by making use of the strong orientational alignment of the

specific graphene samples that we have used, which was within $\pm 1°$. Naïvely, one might expect this to lead to a measurable angular dependence of the friction coefficient, with sharp maxima every 60°, separated by a low friction level for all other angles. There is a simple explanation for the absence of such a signature in Fig. 6.4.

We first point out that the data in Fig. 6.4 show a significant variation in the friction force and that the difference between the average friction coefficients measured in clockwise ($\mu = 0.15$) and counter-clockwise directions ($\mu = 0.25$) suggests the presence of a certain, third-body contact element. This could be an edge effect of the counter sample, introduced by its dicing from the original wafer. Lateral forces and instabilities introduced by such an effect might obscure the increase in friction introduced by a commensurate orientation of the graphene lattices. Another complicating element is the possible presence of water condensates between the contacting surfaces, even though our measurements were conducted in a relatively dry environment (RH = 2%). In addition to these practical difficulties, we find that there is a more intrinsic difficulty in measuring a macroscopic lattice alignment effect.

We first observe that, even in the high-quality CVD-grown graphene that we have employed, the graphene domains still display a range of orientations of $\pm 1°$ with respect to the average orientation angle. This angular range is probably already large enough to 'destroy' the alignment effect, that would lead to a maximum in the friction coefficient, every 60°. As argued in ref. [81], the minimum rotation angle at which this 'destruction' occurs is inversely proportional to the diameter of the contact between the two surfaces. The size that is relevant here is the minimum of three characteristic dimensions, namely (i) the effective diameter of the entire structure, which is in the order of $1\,cm$, (ii) the diameter of the graphene domains, which is typically between 1 and 50 μm, and (iii) the diameter of each microscopic region of 'real', physical contact between the two bodies, which is typically $1\,\mu m$. Obviously, the latter, i.e. $1\,\mu m$, is the more appropriate choice. Even though this seems to be a relatively small diameter, it still corresponds to some 4.000 unit cells of the graphene structure. Hence, the width of the friction peak for each individual microcontact is expected to be as narrow as $0.25\,mrad$ or 0.014° [81].

While this angular width of the alignment effect of a single microcontact should be still within reach of the experimental accuracy of the employed rheometer, we should also take into account the fact that over the full, $1 \times 1\ cm^2$ area, simultaneous contact is made over a large ensemble of such microcontacts. The individual microcontacts are typically sufficiently far apart from each other to be associated with different grains and, hence, to differ in their local graphene orientations by the characteristic $\pm 1°$ width of the orientational distribution. This convolutes the narrow 0.014° peak of a single contact with the full $\pm 1°$ angular width of the domain orientation distribution, which should broaden the measured friction peak to a width of 2° and reduce its height by an equivalent factor 140. Probably, this combination has made the remaining alignment effect too small to show up in Fig. 6.4.

We conclude this section by stressing that the difficulty to observe lattice alignment in the friction forces does not render the structural lubricity effect insignificantly small. On the contrary, in this scenario, structural lubricity is so dominant and leads to such narrow friction peaks, that even when the contacting surfaces are optimally aligned, the $\pm 1°$ angular distribution of their graphene orientations is already wide enough to make most of their microcontacts fully superlubric.

6.4.3 Effect of substrate oxidation on nanoscale friction of graphene

Prolonged exposure to ambient conditions was observed to lead to oxidation of the copper substrate under the graphene. This oxidation was found to proceed via structural defects in the graphene, in particular along the graphene grain boundaries (GGBs). Due to the impermeability of well-ordered graphene [12], the rest of the copper film was not oxidized. AFM measurements (Fig. 6.7, 6.8) conducted on the graphene samples after 2 months of exposure to air, indicated a local increase of the height of the oxidized regions by 1 to 4 nm. The Raman spectra showed that the oxide areas were still covered with low-defect-density graphene.

On top of the threefold reduction in friction that a single graphene monolayer introduced on copper, we find that friction is reduced on average nearly by an additional factor 3 when the copper substrate below the graphene is oxidized. Since copper oxide is a semiconductor, it may introduce electrostatic

forces at the contact interface, in contrast to metals, for which conduction will remove such electrostatic effects. However, it was shown earlier that compensation of the contact potential between the tip and the graphene on a SiC substrate did not result in changes in the friction force [73, 74]. In order to fully exclude electrostatic effects in our case, we should repeat our measurements systematically, with different tips and applied bias voltages.

The observed redshifts of the G- and 2D-bands in the Raman spectra were interpreted as a signature of 0.5 to 1.5% tensile strain in the graphene lattice, due to the increased volume of the substrate (copper oxide) under the graphene [54, 57, 58]. The increase of the I_{2D}/I_G ratio (Fig. 6.6), results from a relatively strong increase of Raman intensity from graphene in the presence of copper oxide, which is simply due to difference in light/matter coupling of the graphene on metal and dielectric surfaces [58]. Unoxidized copper substrate causes strong cancelation of the electric field component of the laser radiation due to its metallic nature. In contrast to that, this cancelation is significantly reduced on the semiconductor copper oxide film, which significantly increases the light coupling with the graphene layer on the oxide. Presumably, the 2D-band of graphene is more sensitive to this effect and its intensity increases more than that of the G-band.

It was suggested earlier that graphene, due to its elastic properties, may slightly lift up from the substrate and snap into contact with the tip due to tip-graphene adhesion, the so-called 'puckering effect' [20, 74, 75]. This effect results in a higher lateral force between the tip and graphene monolayer, because one should now invest extra energy in order to push the bulging graphene fold in the scan direction. This scenario has been used to explain the observed friction contrast between bilayer and single layer graphene [73], because of the higher adhesion of the tip with the latter, and thus the stronger puckering effect [e.g. 75]. Systematic AFM studies for different layered materials showed that this puckering is a universal phenomenon for weakly adhering or freely suspended materials. In turn, it is suppressed for strongly adhering substrates [74]. A reduction of the puckering effect on the copper oxide with respect to unoxidized copper may explain the observed further lowering of the friction force in our experiments. Figure 6.9 provides an artist impression of the puckering effect, superimposed on the topographic landscape that was measured by AFM in Fig. 6.8. The upper picture, with the tip making contact with graphene on the bare copper substrate, shows a

stronger puckering than the lower one, for the tip contacting graphene on the copper oxide island. We recognize several mechanisms that could explain this reduced puckering and, hence, reduced friction on copper oxide.

Due to the tensile strain in the graphene lattice on top of the copper oxide, the wrinkles, created in contact with the tip, should become less pronounced or even disappear. Thus, less energy would be required to move them in the lateral direction, in contrast to unstrained graphene on bare copper.

The next effect directly influences the strength of the puckering effect and involves the adhesion between the graphene and its substrate. The adhesion between graphene and bare copper is extremely modest, which makes it easy to develop a significant puckering effect. In earlier studies [77-79] it was demonstrated that a monolayer graphene exhibits strong adhesion to Al_2O_3 and Si_2O, the adhesion energies being almost equally high as that of graphene on Fe [63]. We expect that the adhesion of graphene on copper oxide can be even stronger, since the adhesion force is known to grow with increasing dielectric constant of the substrate and the value for copper oxide is much higher than that of silicon oxide; $\varepsilon_{Cu_2O} = 18.1$ versus $\varepsilon_{Si_2O} = 3.5$ [77]. Generally, the nanoscale friction of graphene is rather sensitive to the level of adhesion to the substrate, and it becomes significantly lower upon increase of adhesion [80].

Another reason for reduced puckering on the oxide is that a higher substrate roughness may reduce adhesion between the tip and the graphene and thereby suppress the puckering effect between them [76]. The average nanoscale roughness on the graphene on the copper oxide was almost 2 times as large as that on graphene on bare copper; we measured root mean square height variations of $0.7\ nm$ versus $0.4\ nm$, respectively.

Based on the experiments presented in this chapter, we cannot distinguish between these contributions to the reduction of the friction on graphene on copper oxide. For this purpose, additional experiments would be required. For example, comparing friction on transferred graphene on (oxidized) copper with measurements on the strained graphene on the aged, and partly oxidized samples, one should be able to isolate the effect of the tensile strain of the graphene. A comparison of the friction on oxides or oxide regions with different roughness should make it possible to determine the influence of the roughness directly.

Knowing these two contributions, one should be able to estimate the importance of the adhesion effect for this case.

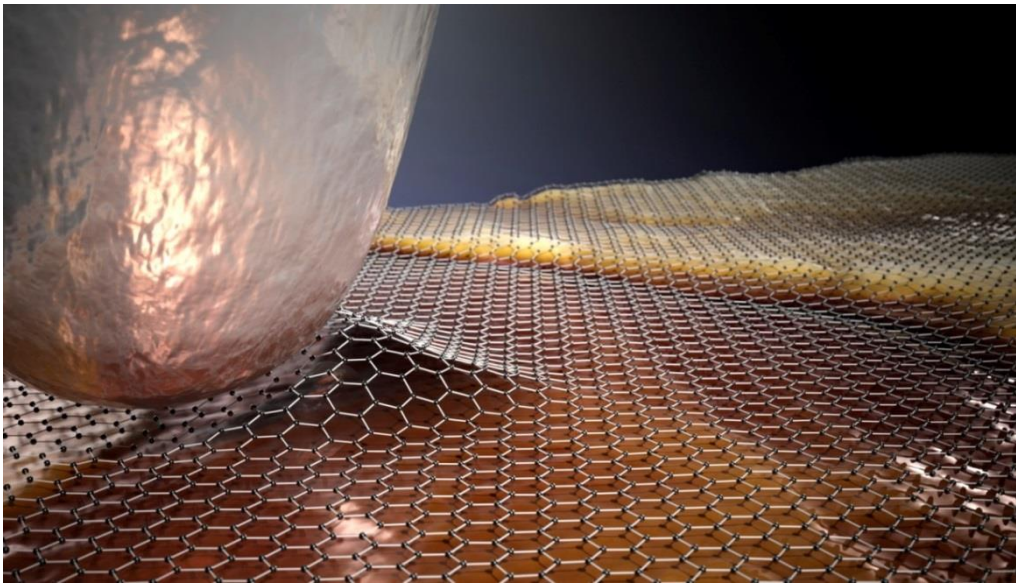

a)

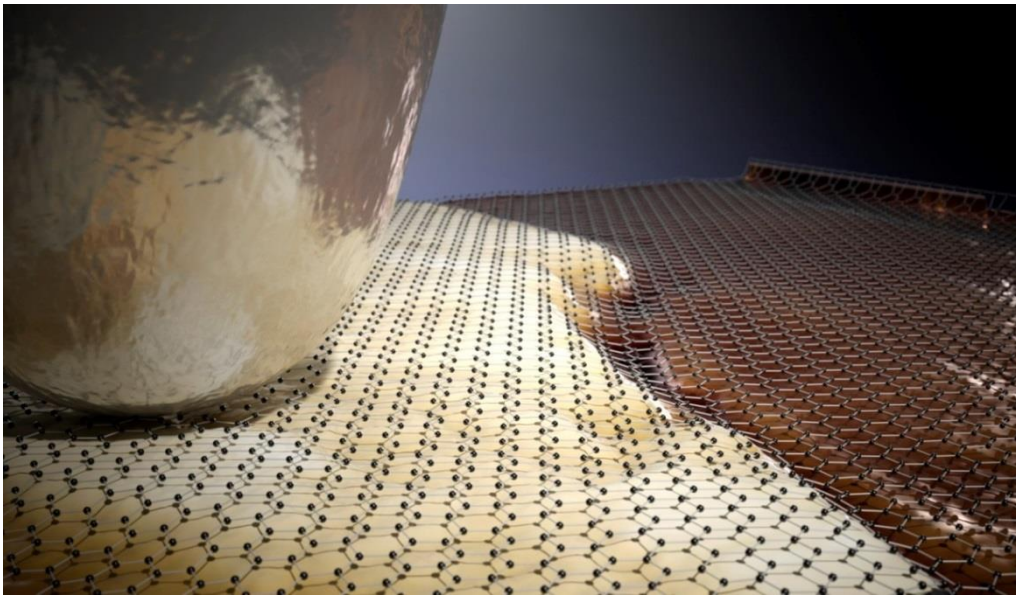

b)

Figure 6.9. Artist impression of the origin of the difference in friction behavior observed in Fig. 8 between graphene on copper and graphene on copper oxide. (a) Loosely adhering graphene on a bare copper substrate tends to bulge up in front of the tip, which leads to higher friction; (b) Tensile strain, stronger graphene-substrate adhesion and larger substrate roughness all suppress the "puckering effect" for graphene on copper oxide; this leads to lower friction.

6.5 Summary

In this chapter, we demonstrated that the presence of a single monolayer of graphene on copper surfaces reduces the sliding friction force between them in ambient by approximately a factor 3 compared to the friction between bare copper surfaces and that it also has a great impact on the static friction behavior. This reduction was shown for surfaces that were completely covered by a monolayer of high-quality graphene. It introduces low surface free energies, minimizes the interaction between contacting asperities, enhances the load capacity and, presumably, causes structural lubricity (superlubricity).

We have not been able to obtain direct experimental evidence that the beneficial effect of the graphene on copper is entirely or partly due to structural lubricity. Angle-dependent measurements did not show a signature of rotational symmetry, which we ascribe to the width of the distribution of domain orientations in the graphene layers that is currently present in even the best large-area graphene samples.

We demonstrated a significant lowering of the friction coefficient measured with friction force microscopy on graphene on top of a locally oxidized copper substrate and we ascribe this to a reduction of the so-called "puckering effect", that otherwise makes the graphene bulge strongly in front of the sliding tip. The increased volume of the copper oxide resulted in tensile strain in the graphene. Next to this tensile strain, also the increased interaction between the graphene and the oxidized substrate and the reduced interaction of the tip with the rougher landscape of the graphene-covered oxide can have made the puckering effect smaller.

Further experiments will be required to distinguish the individual roles of the above effects and to identify other sources of influence on the spectacular, lubricating properties of graphene that were demonstrated here. We believe that our observations may bring new insights in certain technological processes and that they carry the promise to contribute to future developments towards tunable interaction and tunable friction between surfaces.

6.6 Bibliography

1. Novoselov, K.S *et al*. Electric Field effects in Atomically thin carbon films. *Science* **306**, pp. 666-669 (2004)
2. Geim, A.K. & Novoselov, K.S. The rise of graphene. *Nature Materials* **6**, pp. 183-191 (2007)
3. Wallace, P.R. The Band Theory of Graphite. *Physical Review* **71**, pp. 622-634 (1947)
4. Garg, R. *et al*. Work function engeneering in graphene. *Nanomaterials* **4**, pp. 267-300 (2014)
5. Lee, C. *et al*. Measurement of the elastic properties and intrinsic strength of monolayer graphene. *Science* **321**, 358-8 (2008)
6. Xu, X. *et al.* Length-dependent thermal conductivity in suspended single-layer graphene. *Nature Communications* **5**, 3689 (2014)
7. Pop, E., Varshney, V. & Roy, A. Thermal properties of graphene: Fundamentals and applications. *MRS Bulletin* **37**, pp. 1273-1281 (2012)
8. Novoselov *et al.* A roadmap for graphene. *Nature* **490**, pp. 192-200 (2012)
9. Ghosh *et al.* Extremely high thermal conductivity of graphene: Prospects for thermal management applications in nanoelectronic circuits. *Applied Physics Letters* **92**, 151911 (2008)
10. Moser, J., Barreiro, A. & Bachtold, A. Current-induced cleaning of graphene. *arXiv* (2007). doi:10.1063/1.2789673
11. Mayorov, A. *et al.* Micrometer-Scale Ballistic Transport in Encapsulated Graphene at Room Temperature. *Nano Lett* **11**, pp. 2396-2399 (2011)
12. Bunch, S. *et al.* Impermeable Atomic Membranes from Graphene Sheets. *Nano Letters* **8**, pp. 2458-2462 (2008)
13. Chen, S. *et al.* Oxidation Resistance of Graphene-Coated Cu and Cu/Ni Alloy. *ACS Nano* **5**, pp. 1321-1327 (2011)
14. Loh, K., Bao, Q., Ang, P. & Yang, J. The chemistry of graphene. *Journal of Materials Chemistry* **20**, pp. 2277-2289 (2010)
15. Britnell, L. *et al*. Field-Effect Tunneling Transistor Based on Vertical Graphene Heterostructures. *Science* **335**, 947-50 (2012)
16. Schwierz, F. Graphene transistors. *Nature Nanotechnology* **5**, pp. 487-496 (2010)

17. Zhang, H., Gruner, G., & Zhao, Y. Recent advancements of graphene in biomedicine. *Journal of Materials Chemistry B* **1**, 2542 (2013)
18. Wang, X., Zhi, L. & Müllen, K. Transparent, Conductive Graphene Electrodes for Dye-Sensitized Solar Cells. *Nano Letters* **8**, pp. 323-327 (2008)
19. Penkov, O., Kim, H.-J., Kim, H.-J. & Kim, D.-E. Tribology of graphene: A review. *International Journal of Precision Engineering and Manufacturing* **15**, pp. 577-585 (2014)
20. Egberts, P., Han, G., Liu, X., Johnson, C. & Carpick, R. Frictional Behavior of Atomically Thin Sheets: Hexagonal-Shaped Graphene Islands Grown on Copper by Chemical Vapor Deposition. *ACS Nano* **8**, pp. 5010-5021 (2014)
21. Marsden. A.J. *et al*. Friction force microscopy : a simple technique for identifying graphene on rough substrates and mapping the orientation of graphene grains on copper. *Nanotechnology* **24**, 25 (2013)
22. Choi, J.S. *et al*. Friction Anisotropy – Driven Domain Imaging on Exfoliated Monolayer Graphene. *Science* **233**, 607-10 (2011)
23. Li, X. *et al*. Large-Area synthesis of high-quality and uniform graphene films on copper foils. *Science* **324**, pp. 1312-1314 (2009)
24. Li, B., Pan, G., Awan, S. & Avent, N. Techniques for Production of Large Area Graphene for Electronic and Sensor Device Applications. *Graphene and 2D Materials* **1**, pp. 47-58 (2014)
25. Berman, D., Erdemir, A. & Sumant, A. Graphene: a new emerging lubricant. *Materials Today* **17**, pp. 31-42 (2014)
26. Berman, D., Erdemir, A. & Sumant, A. Reduced wear and friction enabled by graphene layers on sliding steel surfaces in dry nitrogen. *Carbon* **59**, pp. 167-175 (2013)
27. Mao, F., Wiklund, U., Andersson, A. & Jansson, U. Graphene as a lubricant on Ag for electrical contact applications. *Journal of Material Science* **50**, pp. 6518-6525 (2015)
28. Kim, K.-S. *et al.* Chemical Vapor Deposition-Grown Graphene: The Thinnest Solid Lubricant. *ACS Nano* **5**, pp. 5107-5114 (2011)
29. Berman, D. *et al*. Macroscale superlubricity enabled by graphene nanoscroll formation. *Science* **348**, pp. 1118-1122 (2015)
30. Hirano, M. Atomistic locking and friction. *Physical Review B* **41**, 11837 (1990)

31. Hirano, M., Shinjo, K., Kaneko, R. & Murata, Y. Anisotropy of frictional forces in muscovite mica. *Physical Review Letters* **67**, pp. 2642-2645 (1991)
32. Shinjo, K. & Hirano, M. Dynamics of friction: superlubric state. *Surface Science* **283**, pp. 473-478 (1993)
33. Hirano, M. *et al*. Observation of Superlubricity by Scanning Tunneling Microscopy. *Physical Review Letters* **78**, 1448 (1997)
34. Martin, J.M., Donnet, C. & Mogne, Th. Superlubricity of MoS2. *Physical Review B* **48**, 10583 (1993)
35. Dienwiebel, M. *et al*. Superlubricity of graphite. *Physical review letters* **92**, 126101 (2004)
36. Liu, Z. *et al*. Observation of Microscale Superlubricity in Graphite. *Physical Review Letters* **108**, 205503 (2012)
37. Koren, E. *et al*. Adhesion and friction in mesoscopic graphite contacts. *Surface Science* **348**, 6235 (2015)
38. Pitenis, A., Dowson, D. & Sawyer, G. Leonardo da Vinci's Friction Experiments: An Old Story Acknowledged and Repeated. *Tribology Letters* **56**, pp. 509-515 (2014)
39. http://appliednanolayers.com/ Visited on 08 February 2017
40. http://repository.upenn.edu/cgi/viewcontent.cgi?article=1000&context=scn_tooldata Visited on 08 February 2017
41. https://www.disco.co.jp/eg/products/blade/vt07.html Visited on 08 February 2017
42. Ying Wang, Y. *et al*. Raman Studies of Monolayer Graphene: The Substrate Effect. *The Journal of Physical Chemistry C* **112**, pp. 10637-10640 (2008)
43. Malard, L.M. *et al*. Raman spectroscopy in graphene. *Physical Reports* **473**, pp. 51-87 (2009)
44. Costa, S. *et al*. Resonant Raman spectroscopy of graphene grown on copper substrates. *Solid State Communications* **152**, pp. 1317-1320 (2012)
45. Platzman, I., Brener, R., Haick, H. & Tannenbaum, R. Oxidation of Polycrystalline Copper Thin Films at Ambient Conditions. *The Journal of Physical Chemistry C* **112**, pp. 1101-1108 (2008)
46. Feng, X., Kwon, S., Park, J. & Salmeron, M. Superlubric Sliding of Graphene Nanoflakes on Graphene. *ACS Nano* **7**, pp. 1718-1724 (2013)

47. Demirbaş, T. & Baykara, M. Nanoscale tribology of graphene grown by chemical vapor deposition and transferred onto silicon oxide substrates. *Journal of Materials Research* **31**, pp. 1914-1923 (2016)
48. Lee, H., Lee, N., Seo, Y., Eom, J. & Lee, S. Comparison of frictional forces on graphene and graphite. *Nanotechnology* **20**, 325701 (2009)
49. Filleter *et al.* Friction and Dissipation in Epitaxial Graphene Films. *Physical Review Letters* **102**, 086102 (2009)
50. Deng, Z., Smolyanitsky, A., Li, Q., Feng, X.-Q. & Cannara, R. Adhesion-dependent negative friction coefficient on chemically modified graphite at the nanoscale. *Nature Materials* **11**, pp. 1032-1037 (2012)
51. Marchetto, D., Feser, T. & Dienwiebel, M. Microscale study of frictional properties of graphene in ultra high vacuum. *Friction* **3**, pp. 161-169 (2015)
52. Marchetto *et al.* Friction and Wear on Single-Layer Epitaxial Graphene in Multi-Asperity Contacts. *Tribology Letters* **48**, pp. 77-82 (2012)
53. Kim, K. *et al.* Multiply folded graphene. *Physical Review B* **83**, 245433 (2011)
54. Duong, D. *et al.* Probing graphene grain boundaries with optical microscopy. *Nature* **490**, pp. 235-239 (2012)
55. Choi, J.L. & Gethin, D.T. Simulation of atomic force microscopy operation via three-dimensional finite element modelling. *Nanotechnology* **20**, 065702 (2009)
56. Cannara, R., Eglin, M. & Carpick, R. Lateral force calibration in atomic force microscopy: A new lateral force calibration method and general guidelines for optimization. *Review of Scientific Instruments* 77, 053701 (2006)
57. Huang, M. *et al.* Phonon softening and crystallographic orientation of strained graphene studied by Raman spectroscopy. *Proceedings of the National Academy of Sciences* **106**, pp. 7304-7308 (2009)
58. Yin, X. *et al.* Evolution of the Raman spectrum of graphene grown on copper upon oxidation of the substrate. *Nano Research* 7, pp. 1613-1622 (2014)
59. Capasso *et al.* Graphene ripples generated by grain boundaries in highly ordered pyrolytic graphite. *Carbon* **68**, pp. 330-336 (2014)

60. Palacio, M. & Bhushan, B. Normal and Lateral Force Calibration Techniques for AFM Cantilevers. *Critical Reviews in Solid State and Materials Sciences* **35**, pp. 73-104 (2010)
61. Singh, E. *et al.* Graphene Drape Minimizes the Pinning and Hysteresis of Water Drops on Nanotextured Rough Surfaces. *ACS Nano* **7**, pp. 3512-3521 (2013)
62. Meyer, E., Overney, R.M., Dransfeld, K., & Gyalog T., Nanoscience: Friction and Rheology on the Nanometer Scale. *World Scientific Publishing*, Singapore (1998)
63. Restuccia, P. & Righi, M.C. Tribochemistry of graphene on iron and its possible role in lubrication of steel. *arXiv* (2016). doi:10.1016/j.carbon.2016.05.025
64. Klemenz, A. *et al.* Atomic Scale Mechanisms of Friction Reduction and Wear Protection by Graphene. *Nano Letters* **14**, pp. 7145-7152 (2014)
65. Zhang, Q., Diao, D. & Yang, L. Dangling bond induced cross-linking model in nanoscratched graphene layers. *Surface and Coatings Technology* **237**, pp. 230-233 (2013)
66. Berman, D., Deshmukh, S., Sankaranarayanan, S., Erdemir, A. & Sumant, A. Extraordinary Macroscale Wear Resistance of One Atom Thick Graphene Layer. *Advanced Functional Materials* **24**, pp. 6640-6646 (2014)
67. Baumberger, T. & Caroli, C. Solid friction from stick slip down to pinning and aging. *ArXiv,* doi: 10.1080/00018730600732186 (2005)
68. Lahiri, J. *et al.* Graphene growth and stability at nickel surfaces. *New Journal of Physics* **13**, 025001 (2011)
69. He, Y. *et al*. Anomalous interface adhesion of graphene membranes. *Scientific Reports* **3**, 2660 (2013)
70. Wintterlin, J. & Bocquet, M.-L. Graphene on metal surfaces. *Surface Science* **603**, pp. 1841-1852 (2009)
71. Das, S., Lahiri, D., Lee, D.-Y., Agarwal, A. & Choi, W. Measurements of the adhesion energy of graphene to metallic substrates. *Carbon* **59**, pp. 121-129 (2013)
72. Won, M.-S., Penkov, O. & Kim, D.-E. Durability and degradation mechanism of graphene coatings deposited on Cu substrates under dry contact sliding. *Carbon* **54**, pp. 472-481 (2013)

73. Filleter, T. & Bennewitz, R. Structural and frictional properties of graphene films on SiC(0001) studied by atomic force microscopy. *Physical Review B* **81**, 155412 (2010)
74. Lee, C. *et al* Frictional Characteristics of Atomically Thin Sheets. *Science* **328**, pp. 76-80 (2010)
75. Lee, C. *et al.* Elastic and frictional properties of graphene. *Physica Status Solidi (b)* **246**, pp. 2562-2567 (2009)
76. Spear, J.C. *et al*. The influence of nanoscale roughness and substrate chemistry on the frictional properties of single and few layer graphene. *Nanoscale* 7, 10021 (2015)
77. Song, S. & Cho, B. Investigation of interaction between graphene and dielectrics. *Nanotechnology* **21**, 335706 (2010)
78. Koenig, S., Boddeti, N., Dunn, M. & Bunch, S. Ultrastrong adhesion of graphene membranes. *Nature Nanotechnology* **6**, pp. 543-546 (2011)
79. Das, S. *et al*. Interfacial bonding characteristics between graphene and dielectric substrates. *Nanotechnology* **25**, 045707 (2014)
80. Berman, D., Erdemir, A., Zinovev, A. & Sumant, A. Nanoscale friction properties of graphene and graphene oxide. *Diamond and Related Materials* **54**, pp. 91-96 (2015)
81. Verhoeven, G., Dienwiebel, M. & Frenken, J. Model calculations of superlubricity of graphite. *Physical Review B* **70**, 165418 (2004)
82. De Wit, M. Antonov, P., van Baarle, D. & Frenken., J. On slippery ground: towards superlubricity of graphene. *MSc Thesis*, University of Leiden (2013)
83. Strictly speaking, the rotation symmetry of the graphite lattice is 120° rather than 60°. However, it is only in the local stacking of the layers that the symmetry is broken from 60° to 120°, which implies that two contacting graphite lattices do lock in every 60° and that there may be a modest modulation in the strength of this effect, such that even multiples of 60° lead to somewhat more friction than odd multiples.